

# Semiconducting $\alpha'$ -borophene nanoribbon for high-efficiency spin-Seebeck diodes

F. Ghasemzadeh and M. Esmaeilzadeh\*

*Department of Physics, Iran University of Science and Technology, Narmak, Tehran 16844, Iran*

M. Farokhnezhad<sup>†</sup>

*Department of Physics, School of Science,  
Shiraz University, Shiraz 71946-84795, Iran*

(Dated: December 20, 2024)

arXiv:2412.14840v1 [cond-mat.mes-hall] 19 Dec 2024

## Abstract

The semiconducting  $\alpha'$ -borophene nanoribbon ( $\alpha'$ -BNR) due to its incredible properties such as high stability and great mobility of carriers demonstrates high-efficiency in thermoelectric devices. These properties enable us to produce the spin current by a temperature gradient with lower energy consumption technology. In this research, the spin-dependent Seebeck effects are studied in a zigzag  $\alpha'$ -borophene nanoribbon with two leads magnetized by ferromagnetic (FM) insulators. The thermoelectric calculations are performed for a  $\alpha'$ -BNR FM/Normal/FM junction using the tight-binding (TB) formalism in combination with the non-equilibrium Green's function method (NEGF). A pure spin-dependent current due to the breaking of the electron-hole symmetry is induced in the system by a temperature gradient so that it can act as a spin-Seebeck diode. Moreover, the negative differential spin-Seebeck effect can be observed in this device due to the compensation of thermal spin in the spin-dependent currents. Finally, we have studied the effect of temperature on the charge and spin power factors in  $\alpha'$ -BNR. A significant decline in power factor is primarily arises from a reduction in the magnitude of thermopower near the Fermi level. Our findings demonstrate that the  $\alpha'$ -BNR has a higher power factor compared to its rivals e.g., graphene and silicene. This is attributed to the semiconducting nature and high asymmetry between electrons and holes in the  $\alpha'$ -BNR. The exceptional features of  $\alpha'$ -BNR makes it a very suitable choice for using in thermoelectric devices.

## I. INTRODUCTION

The field of spin caloritronics [1–5], which combines spintronics with thermoelectronics, has attracted considerable interest due to its potential in improving energy efficiency [6–8]. Thermoelectric devices are capable of producing a spin current under a temperature gradient, even without an external electric field. The control of spin currents is accomplished by the regulation of thermal currents. Under certain circumstances, the spin-Seebeck effect has the potential to induce a perfect spin current inside selective materials by breaking of the electron-hole spin symmetry [9, 10]. The observed phenomenon is contingent upon the Seebeck coefficients, which illustrate contrasting polarities for spin up and spin down. This

---

\* mahdi@iust.ac.ir

† m.farokhnezhad@saadi.shirazu.ac.ir

intrinsic property of materials plays a pivotal role in the manufacturing of nanodevices that demonstrate exceptional efficiency and longevity with low power consumption. The low-dimensional nanostructures such as two-dimensional (2D) materials and nanoribbons due to the low phonon thermal conductivity and the high spin-dependent Seebeck coefficients possess higher thermoelectric efficiency than bulk materials, so that they have received noticeable attention [11–13].

Borophene, a planar structure comprised of boron atoms [14], has attracted considerable attention among researchers owing to its diverse arrangements and notable functionalities including physical, electronics, optical transparency, and high electron mobility [15–21]. This material is being acknowledged as a potential competitor to graphene. Furthermore, the distinct band gap shown by different phases of borophene imparts advantageous practical properties in contrast to the gapless nature of graphene [17, 18, 22, 23]. Upon comparing graphene with the 8B-Pmmn phase, it becomes evident that the latter has a superior carrier mobility of  $10^6 \text{ cm}^2\text{V}^{-1} \text{ s}^{-1}$  at room temperature conditions (The carrier mobility of graphene is  $15000 \text{ cm}^2\text{V}^{-1} \text{ s}^{-1}$ ) [24, 25]. The buckled structure of borophene,  $\alpha'$ -phase, with hollow hexagons in its configuration due to the high cohesive energy, high mobility of electrons, and semiconducting behavior makes the  $\alpha'$ -boron sheets an important system in nanotechnology [23, 26–29]. The high stability of  $\alpha'$ -boron is due to the weak buckling which is made of the hybridization between  $\pi$ -bond and  $s + p_{x,y}$  orbitals.

The thermal transport property of the  $\alpha'$  sheet through the first-principles calculations based on the density functional theory (DFT) is studied by Xiao *et al.*. They found the lattice thermal conductivity of the  $\alpha'$  sheet is about  $14.34 \text{ Wm}^{-1}\text{K}^{-1}$  which is much smaller than that of graphene about  $3500 \text{ Wm}^{-1}\text{K}^{-1}$  [30]. This low thermal conductivity of the  $\alpha'$  sheet supports a higher figure of merit than that of graphene.

Zhang *et al.*, investigated the outstanding stability of the  $\alpha'$ -boron sheets with semiconductor characteristics by employing both the tight-binding (TB) model and first-principles calculations. Their results illustrate due to the small effective masses of electrons and holes, the carrier mobility in the  $\alpha'$ -boron sheet is high which can be an appealing candidate for manufacturing 2D field effect transistors (FETs). Low Ohmic contact resistance between the semiconducting  $\alpha'$ -boron channel and the metallic borophene as the electrodes was another accomplishment of their studies [26].

Recently, the  $\alpha'$ -4H-borophene ( $\text{B}_8\text{H}_4$ ) was successfully synthesized and the morpholo-

gies of this structure were characterized via scanning electron microscopy (SEM) [31, 32]. The  $B_8H_4$  and graphene heterostructure through the ultrahigh sensitivity, fast response and long-time stability can be applied in sensors and wearable electronics [33]. The potential application of hydrogenated borophene ( $B_8H_4$ ) in FETs based on the first-principles calculations was determined by Sang *et al.*. They also showed that the electronic properties of monolayer  $B_8H_4$  can be tuned under strain engineering in the ballistic transport regime [34].

The one-dimensional (1D) structure of materials, nanoribbons, has also shown superior properties in the fields of electronic and thermoelectric transport. There is a lot of research on the thermoelectric properties of different nanoribbons in recent years [35–40]. Metals were the initial materials investigated for thermoelectric applications. Their large Seebeck coefficients are due to the existence of the band gap which breaks the electrons and holes symmetry. This feature persuades us that materials with semiconducting behavior can have high efficiency performance in thermoelectric applications with high power factor (PF). Moreover, large carrier mobility in semiconducting materials results in the high thermoelectric PF due to the low electron-electron and electron-phonon interactions [41]. The thermoelectric properties of the semiconductor  $\alpha'$ -borophene nanoribbon ( $\alpha'$ -BNR) have not been calculated yet, so we intend to study the thermopower and spin-Seebeck effect in  $\alpha'$ -BNRs in more detail. In this paper, we have designed a thermoelectric device composed of ferromagnetic (FM) electrodes and a normal channel. The calculation of spin-dependent currents and the spin thermopower are performed via the non-equilibrium Green's function (NEGF) method and the Landauer-Buttiker formula. The article is arranged as follows: in Sec. II we present our system and model which are employed to calculate the thermoelectric properties. The results of this study are summarized in Sec. III. Finally, we conclude our results and findings in Sec. IV.

## II. THEORETICAL MODEL

Our setup in this study, is depicted in Fig. 1. We designed a FM/Normal/FM junction made of a zigzag  $\alpha'$ -BNR. The magnetization of both electrodes is postulated to be equivalent, and the magnetic arrangement of the right and left electrodes aligns along the z-axis ( $M_R = M_L = M_z$ ). The tight-binding (TB) method using the NEGF formalism [42] has been used to calculate the thermoelectric properties of the zigzag  $\alpha'$ -BNR.

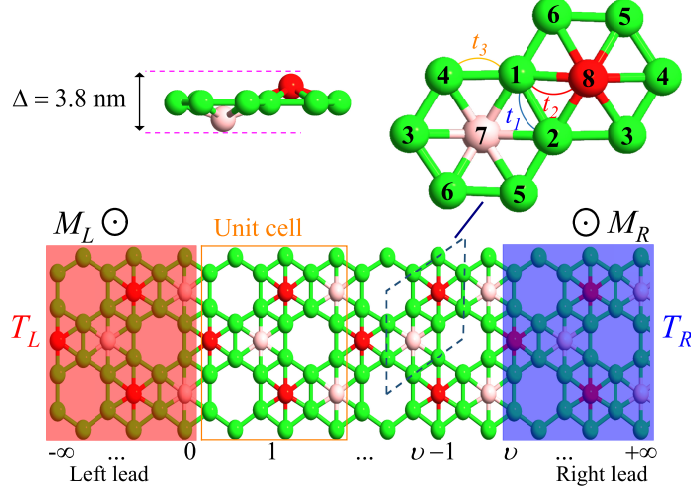


FIG. 1. Schematic depicting of a zigzag  $\alpha'$ -BNR junction consisting of an scattering part (channel) and the same two semi-infinite FM leads. The magnetic moment of the two FM electrodes is aligned at the z-axis ( $M_R = M_L = M_z$ ).  $T_L$  and  $T_R$  denote the temperatures of the left and right leads, respectively. The blue dashed line represents the primitive cell. The hopping energies between the first nearest-neighbor (NN) atoms are exhibited by  $t_1$ ,  $t_2$  and  $t_3$ . The channel includes  $\nu$  unit cells, and each unit cell consists of a total of  $N$  boron atoms. Here, the number of atoms in each unit cell are 30 and  $M_z=0.098$  eV.

The total Hamiltonian ( $H_T$ ) of the system can be written as follows:

$$H_T = H_C + H_L + H_R, \quad (1)$$

where  $H_C$ ,  $H_L$  and  $H_R$  are the Hamiltonian of the scattering area (channel), the left and right FM electrodes, respectively. The tight-binding Hamiltonian of each parts (channel, left and right electrodes) is represented as:

$$H_C = -t \sum_{\langle i,j \rangle, \alpha} c_{i\alpha}^\dagger c_{j\alpha} + \sum_{\langle i,j \rangle, \alpha} \varepsilon_i c_{i\alpha}^\dagger c_{j\alpha}, \quad (2)$$

$$H_L = H_R = -t \sum_{\langle i,j \rangle, \alpha} c_{i\alpha}^\dagger c_{j\alpha} + M_z \sum_{i, \alpha} c_{i\alpha}^\dagger \sigma_z c_{i\alpha} \quad (3)$$

where  $t$  in the first term is the hopping energy between the nearest-neighbor (NN) sites. Also  $\langle i, j \rangle$  expresses the sum over NN hopping sites,  $c_{i\alpha}^\dagger$  and  $c_{i\alpha}$  stand for the creation and annihilation operators, which creates and annihilates an electron at site  $i$  with spin  $\alpha$ , respectively.

The hopping parameters  $t_1$  (between the two atoms of the adjacent sides of the hexagonal, atom 1 to 2),  $t_2$  (between the central atom with each corner atom, atom 1 to 8), and  $t_3$  (between the two atoms on the hollow hexagon's sides, atom 1 to 4) is shown in Fig. 1. The second term denotes the on-site energy  $\varepsilon_i$ . There are two different types of on-site energy where  $\varepsilon_1$  and  $\varepsilon_2$  are the on-site energy of fivefold (five-bonding) (1 and 2) and sixfold (six-bonding) atoms (7 and 8), respectively.

The fitted tight-binding model parameters are set as [26]:

$$t_1 = 2.55 \text{ eV}, \quad t_2 = 2.05 \text{ eV}, \quad t_3 = 2.19 \text{ eV},$$

$$\varepsilon_1 = -1.90 \text{ eV}, \quad \varepsilon_2 = -2.65 \text{ eV}. \quad (4)$$

The last term in Eq. 3, which is created by the proximity of ferromagnetic materials with the leads [43], is an exchange field with a strength of  $M_z$ . Also,  $\sigma_z$  is the z-component of Pauli's spin matrices. In the following, the spin-dependent conductance of  $\alpha'$ -BNRs can be calculated using the NEGF method: The surface retarded Green's functions of the left and right leads are obtained through the use of an iterative technique called Lopez-Sancho's algorithm [44, 45]:

$$g_{0,0}^L(E) = [(E + i\eta)\mathbf{I} - H_{0,0} - H_{-1,0}^\dagger \tilde{T}]^{-1}, \quad (5)$$

$$g_{\nu,\nu}^R(E) = [(E + i\eta)\mathbf{I} - H_{\nu,\nu} - H_{\nu,\nu+1}T]^{-1}, \quad (6)$$

where  $\mathbf{I}$  is an identity matrix,  $\eta$  is an infinitesimal positive real number,  $H_{0,0}$  ( $H_{\nu,\nu}$ ) is the Hamiltonian matrix of the assumed unit cell at site 0 ( $\nu$ ) of the device, and  $H_{-1,0}$  ( $H_{\nu,\nu+1}$ ) is the coupling matrix of the left-hand (right-hand) adjacent cells at sites -1 and 0 ( $\nu$  and  $\nu + 1$ ).

In this study, the left lead has been considered the same as the right one;  $H_{0,0} = H_{\nu,\nu}$  and  $H_{-1,0} = H_{\nu,\nu+1}$ .

The transfer matrices  $T$  and  $\tilde{T}$  are determined through the following sequences [44–46]:

$$T = \tilde{t}_0 + \tilde{t}_0 t_1 + \tilde{t}_0 \tilde{t}_1 t_2 + \dots + \tilde{t}_0 \tilde{t}_1 \tilde{t}_2 \dots t_n, \quad (7)$$

$$\tilde{T} = t_0 + t_0 \tilde{t}_1 + t_0 t_1 \tilde{t}_2 + \dots + t_0 t_1 t_2 \dots \tilde{t}_n, \quad (8)$$

where the definition of  $t_i$  and  $\tilde{t}_i$  through the recursion relations can be written as:

$$t_i = (\mathbf{I} - t_{i-1} \tilde{t}_{i-1} - \tilde{t}_{i-1} t_{i-1})^{-1} t_{i-1}^2, \quad (9)$$

$$\tilde{t}_i = (\mathbf{I} - t_{i-1}\tilde{t}_{i-1} - \tilde{t}_{i-1}t_{i-1})^{-1}\tilde{t}_{i-1}^2, \quad (10)$$

and

$$t_0 = [(E + i\eta)\mathbf{I} - H_{00}]^{-1}H_{-10}^\dagger, \quad (11)$$

$$\tilde{t}_0 = [(E + i\eta)\mathbf{I} - H_{00}]^{-1}H_{-10}. \quad (12)$$

The above iteration procedure is repeated until  $t_n$  and  $\tilde{t}_n$  have a tendency to a quite small arbitrary amount.

Now, the surface Green's function inside the transport channel can be obtained step by step through the sampling of the scattering region as a part of the right lead returning from  $l = \nu$  to  $l = 2$ , using the recursion relation as follows [45]:

$$g_{l,l}^{R\alpha}(E) = [(E + i\eta)\mathbf{I} - H_{l,l} - H_{l,l+1}g_{l+1,l+1}^{R\alpha}H_{l,l+1}^\dagger]^{-1}. \quad (13)$$

Furthermore, the total  $g_{11}^\alpha$  Green's function can be written as [47]:

$$g_{11}^\alpha = [(E + i\eta)\mathbf{I} - H_{11} - \Sigma_L^\alpha - \Sigma_R^\alpha]^{-1}, \quad (14)$$

Also, the self-energy of the left ( $\Sigma_L^\alpha$ ) and the right ( $\Sigma_R^\alpha$ ) leads are defined by:

$$\Sigma_L^\alpha = H_{01}^\dagger g_{00}^{L\alpha} H_{01}, \quad (15)$$

$$\Sigma_R^\alpha = H_{12} g_{22}^{R\alpha} H_{12}^\dagger. \quad (16)$$

Density of states for  $\alpha'$ -BNR can be calculated using the Green's function as follows:

$$\rho(E) = -\frac{1}{\pi} \text{Im}[\text{Tr}(g_{11}(E))], \quad (17)$$

Finally, the spin-dependent conductance of  $\alpha'$ -BNR can be written by using the the Landauer-Büttiker formula [47, 48]:

$$G^\alpha(E) = \frac{e^2}{h} T^\alpha(E), \quad \alpha = \uparrow, \downarrow. \quad (18)$$

where  $T^\alpha(E)$  is the spin-dependent transmission coefficient as follows [49, 50]:

$$T^\alpha(E) = \text{Tr}[\Gamma_L^\alpha(E)g_{11}^\alpha(E)\Gamma_R^\alpha(E)(g_{11}^\alpha(E))^\dagger] \quad (19)$$

The broadening matrix which represents the coupling interaction between the channel and the left (right) lead can be defined as follows:

$$\Gamma_{L(R)}^\alpha = i (\Sigma_{L(R)}^\alpha - (\Sigma_{L(R)}^\alpha)^\dagger). \quad (20)$$

The induced spin-dependent current through the temperature gradient  $\Delta T = T_L - T_R$  between the left and right leads is represented using the Landauer-Büttiker formula [51]:

$$I^\alpha = \frac{e}{h} \int_{-\infty}^{+\infty} T^\alpha(E) [f_L(E, T_L) - f_R(E, T_R)] dE, \quad (21)$$

The spin current ( $I_S = I^\uparrow - I^\downarrow$ ) and charge current ( $I_C = I^\uparrow + I^\downarrow$ ) are the difference and sum of the  $I^\uparrow$  and  $I^\downarrow$ , respectively. Further,  $T^\alpha(E)$  is the spin-dependent transmission coefficient,  $f_L$  and  $f_R$  are the Fermi-Dirac distribution function at temperature  $T_L$  and  $T_R$ , respectively. The Fermi-Dirac distribution function at temperature  $T$  and energy  $E$  is defined as follows:

$$f(E, T) = \frac{1}{1 + e^{(E-E_F)/k_B T}}, \quad (22)$$

where  $E_F$  and  $k_B$  are the Fermi energy and Boltzmann constant, respectively.

The spin-Seebeck thermopower coefficient in the ballistic regime is given by [51]:

$$S^\alpha(E_F, T) = -\frac{1}{|e|T} \frac{L_{1\alpha}(E_F, T)}{L_{0\alpha}(E_F, T)}, \quad (23)$$

where the spin-dependent function  $L_{n\alpha}(E_F, T)$  is defined as follows [51]:

$$L_{n\alpha}(E_F, T) = -\frac{1}{h} \int_{-\infty}^{+\infty} T^\alpha(E) \frac{\partial f(E, T)}{\partial E} dE, \quad (24)$$

and the derivative of the Fermi distribution function concerning energy is:

$$\frac{\partial f(E, T)}{\partial E} = -\frac{1}{k_B T} f(E, T) (1 - f(E, T)). \quad (25)$$

Furthermore, the spin and the charge thermopower coefficients can be written as [52]:

$$S_s = S^\uparrow - S^\downarrow \quad (26)$$

$$S_c = \frac{(S^\uparrow + S^\downarrow)}{2} \quad (27)$$

Eventually, the important property known as the spin (charge) power factor in thermoelectric is given by:

$$PF_{s(c)} = S_{s(c)}^2 \sigma_{s(c)} \quad (28)$$

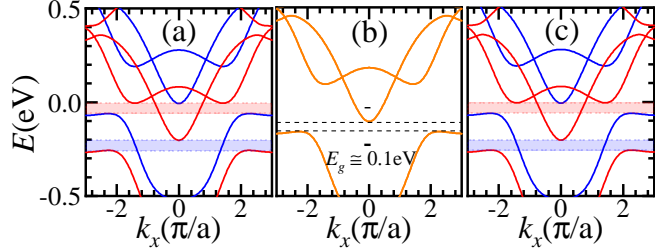


FIG. 2. The band structure (a) for the left lead, (b) for the channel, and (c) for the right lead of a  $\alpha'$ -BNR junction with  $N = 30$ ,  $M_z = 0.098$  eV with parallel configuration in the two leads. The blue and red solid lines are for the spin up and down bands, respectively. The spin up and down bands are degenerate in (b) as shown by the orange solid lines.

where  $\sigma_{s(c)}$  are the spin and charge conductivity of the system and can be obtained as follows [52]:

$$\sigma_s = |\sigma^\uparrow - \sigma^\downarrow| \quad (29)$$

$$\sigma_c = \sigma^\uparrow + \sigma^\downarrow \quad (30)$$

where the spin-dependent conductivity is given by:

$$\sigma^\alpha = e^2 L_{0\alpha}. \quad (31)$$

### III. RESULTS AND DISCUSSION

When the right and left leads are magnetized by the ferromagnetic insulator substrates arranged in a parallel configuration, the exchange magnetic fields with the strength of  $M_z = 0.098$  eV are induced on both leads in a same direction along the z-axis. We have depicted the band structure of the left lead, the channel and the right lead, respectively, under a magnetization with a strength of  $M_z = 0.098$  eV in both leads with a parallel spin configuration (see Fig. 2(a)-(c)). As illustrated in Figs. 2(a) and 2(c), due to the breaking time-reversal symmetry (TRS) through the use of an exchange magnetic field, the spin-up and spin-down levels are split and move in opposite directions.

The spin up and spin down energy levels of the electrons are determined by blue and red solid lines, respectively. The blue and red arrows stand for the spin up and spin down orientations in both leads. As can be seen in the range of energy  $-0.06$  eV  $< E < 0$  eV, the spin down electrons can flow through the system, while in the range of energy  $-0.26$

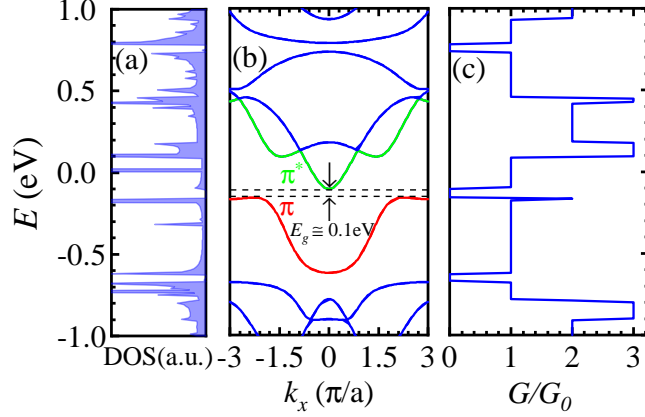


FIG. 3. (a) DOS (b) the band structure (c) and transmission function of the zigzag  $\alpha'$ -BNR in the FM state. The Van Hove singularities can be observed clearly in the DOS. The red and green solid lines denote the valence and conduction bands, respectively. The magnetisation is  $M_z = 0.098$  eV.

$eV < E < -0.2$  eV, the spin up electrons pass through the channel, which is a barrier for the spin down electrons. The  $\alpha'$ -borophene nanodevice shows a half-metallicity characteristic because in one spin orientation has simultaneously a metallic state and an insulating state for the other electrons in the opposite spin direction. In the channel, the bands are degenerate and depicted by the orange solid lines, and the band gap of the  $\alpha'$ -BNR is about  $E_g = 0.1$  eV. The density of states (DOS), band structure and transmission spectrum of the  $\alpha'$ -BNR device have been shown in Fig. 3.

The sharp peaks in DOS are indicative of the Van Hove singularities in our one-dimensional system which are associated with the extremum points in the band structure and DOS follows the band structure well (see Figs. 3(a) and 3(b)). Fig. 3(b) illustrates that the valence band maximum (red line) and conduction band minimum (green line) around the Fermi energy level are affected by the contributions of the two bonding  $\pi$  and  $\pi^*$  antibonding bands. The semiconducting behavior of the  $\alpha'$ -BNR is also approved by the transmission, which is in good agreement with the band structure. Furthermore, the number of energy levels defines the transport channels at each energy level. The number of transmission channels in the energy range of  $-0.09$  eV  $< E < 0.08$  eV is one, whereas it is zero in the energy region between  $-0.15$  and  $-0.1$  eV.

The spin-dependent Seebeck thermopower versus the Fermi energy at  $T = 100, 200,$  and  $300$  K with the parallel configuration of magnetization  $M_z = 0.098$  eV has been illustrated in

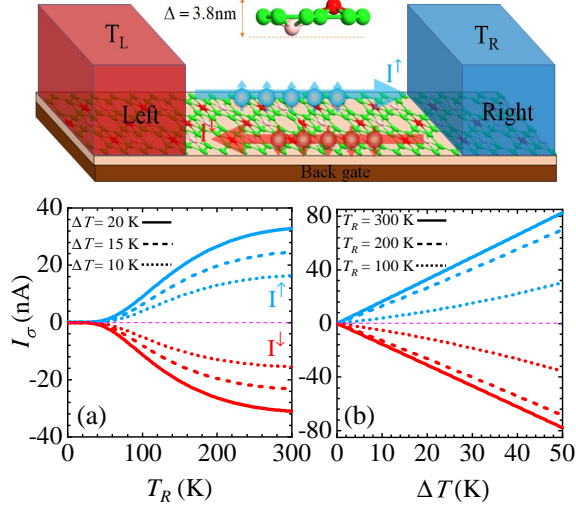


FIG. 4. (a) The Spin-dependent Seebeck thermopower as a function of the Fermi energy for: (a)  $T = 100$  K, (b)  $T = 200$  K, (c)  $T = 300$  K. The green and purple lines are for  $S^\uparrow$  and  $S^\downarrow$ , respectively. The magnetisation is  $M_z=0.098$  eV.

Fig. 4. It can be seen that the spin-up thermopower ( $S^\uparrow$ ) and the spin-down thermopower ( $S^\downarrow$ ) exhibit similar characteristics in the vicinity of Fermi energy. They are displaced in opposite directions, resulting in noticeable spin splitting. As the temperature ( $T$ ) is increased up to the ambient temperature, the spin-dependent Seebeck thermopower becomes broader, and the maximum absolute value of the spin-up thermopower ( $S^\uparrow$ ) and the spin-down thermopower ( $S^\downarrow$ ) are dramatically decreased to  $198$  and  $203 \mu\text{V K}^{-1}$ , respectively.

The signs of the spin-up thermopower and spin-down thermopower specify the system characteristics. The transport channel acts as a p-type doping (n-type doping) when the spin-dependent Seebeck thermopower ( $S^\alpha$ ) has a positive (negative) sign. Furthermore, we can observe a noteworthy property in  $E_F = -0.13$  eV where  $S^\uparrow = -S^\downarrow$ , in which the magnitude of the spin-up and spin-down currents are the same but flow in opposite directions, so the electrons and holes compensate each other. At this neutral point, where the spin-Seebeck effect occurs, the charge current is zero, while the spin current has the maximum value, and a pure spin current flows through the system.

The spin and charge Seebeck coefficients versus the Fermi energy for different temperatures are shown in Fig. 5. As can be seen, the spin-Seebeck coefficient decreases with increasing temperature. The spin Seebeck coefficient has a maximum value for different

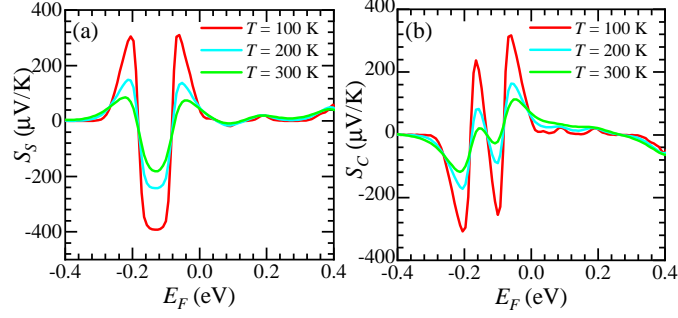


FIG. 5. (a) Spin thermopower and (b) charge thermopower as a function of the Fermi energy for different values of temperature.  $T = 100$  K,  $T = 200$  K, and  $T = 300$  K. The magnetisation is  $M_z = 0.098$  eV.

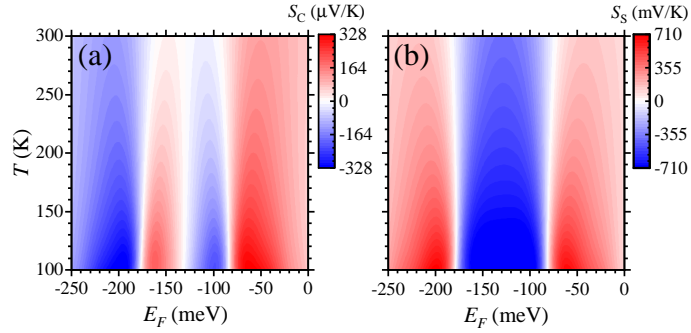


FIG. 6. The contour plots of (a) charge and (b) spin Seebeck coefficients of  $\alpha'$ -BNR as functions of the Fermi energy and temperature. The magnetisation is  $M_z = 0.098$  eV.

temperatures at the Fermi energy of  $-0.13$  eV, and the charge Seebeck coefficient is zero at this energy, simultaneously. We can also adopt a net charge current just through the temperature difference ( $\Delta T$ ) in the system. At the specific Fermi energy ( $E_F = -0.08$  eV), a pure electronic current flows through the device from the left lead with a higher temperature to the right lead with a lower one, so by tuning the Fermi energy, we can get a pure charge or spin current in the system.

Fig. 6 illustrates the contour plots of the charge and spin thermopowers as functions of Fermi energy and temperature. According to Fig. 6(a), when the charge Seebeck coefficient for a range of temperatures at the Fermi energy of  $-0.13$  eV is zero, the spin Seebeck coefficient (see Fig. 6(b)) is maximum. Furthermore, the charge and spin Seebeck coefficients diminish as the temperature increases. These results align with the earlier findings.

To further understand, we demonstrated the spin-dependent currents versus the temperature

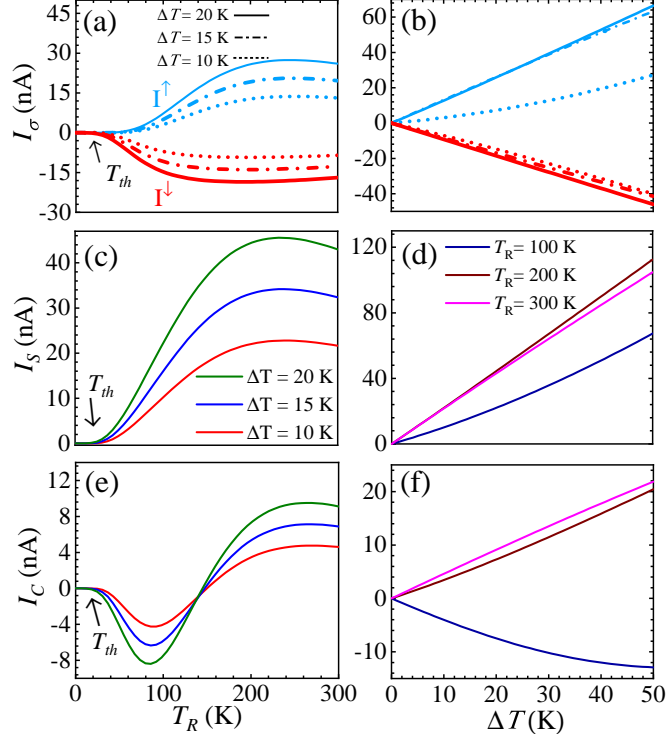


FIG. 7. The spin-dependent currents  $I^\uparrow$  and  $I^\downarrow$  as a function of the right lead temperature  $T_R$  of the zigzag  $\alpha$ -BNR with the temperature difference  $\Delta T = T_L - T_R$ . (b)  $I^\uparrow$  and  $I^\downarrow$  versus  $\Delta T$  with  $T_R = 100, 200,$  and  $300$  K. (c and d) The total spin currents  $I_S (= I^\uparrow - I^\downarrow)$  versus  $T_R$  and  $\Delta T$ , respectively. (e and f) The net electron currents  $I_C = (I^\uparrow + I^\downarrow)$  versus  $T_R$  and  $\Delta T$ , respectively. The magnetisation is  $M_z = 0.098$  eV.

of the right lead ( $T_R$ ) with different  $\Delta T = 10, 15,$  and  $20$  K ( $\Delta T = T_L - T_R$ ). As shown in Fig. 7(a) before the threshold temperature ( $T_{th} = 42$  K), the spin-up and spin-down currents at lower than this value are close to zero, and the spin-dependent currents, driven by the temperature gradient, flow in opposite directions with positive and negative orientations, respectively.

As the absolute magnitudes of the spin-up and spin-down currents are nearly the same, a pure spin-dependent Seebeck effect occurs in the system, and it can act as an ideal spin-Seebeck diode (SSD). Also, as can be seen in Fig. 7(a), the spin-dependent currents ( $I^\uparrow$  and  $I^\downarrow$ ) are boosted by increasing the temperature of the right lead ( $T_R$ ). However, the spin-up current ( $I^\uparrow$ ) and the spin-down current ( $I^\downarrow$ ) versus  $\Delta T$ , with different  $T_R$  have been depicted in Fig. 7(b). The  $I^\uparrow$  and  $I^\downarrow$  increase linearly in opposite directions when  $\Delta T$  enhances from 0 to 50 K. We have also calculated the spin current ( $I_S = I^\uparrow - I^\downarrow$ ) versus  $T_R$  and  $\Delta T$  in

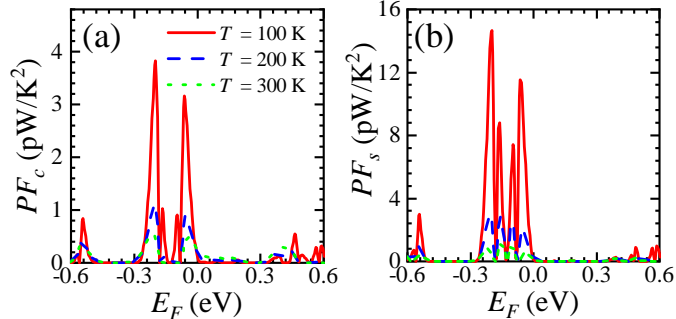


FIG. 8. (a)The charge and (b) spin power factors as a function of the Fermi energy for different temperatures  $T = 100, 200,$  and  $300$  K with  $N = 30$ . The magnetisation is  $M_z = 0.098$  eV.

Figs. 7(c) and 7(d), respectively. It can be observed in a critical temperature,  $T_{th}$ , the spin current ( $I_S$ ) increases dramatically, and by increasing the  $\Delta T$ ,  $I_S$  increases linearly, which makes it a good candidate for manufacturing spin Seebeck effect (SSE) devices.

The behavior of the charge current ( $I_C = I^\uparrow + I^\downarrow$ ) versus  $T_R$  and  $\Delta T$  has been shown in Figs. 7(e) and 7(f), respectively. The charge current versus  $T_R$  is zero up to  $T \leq T_{th}$  and after that,  $I_C$  gets a negative value and reaches a maximum absolute magnitude at about  $T_R = 100$  K, where in this range of temperature the charge current flows from the drain to the source. At a critical temperature of  $T_C = 186$  K,  $I_C$  becomes zero, and then its direction changes and it gains a positive value (see Fig. 7(e)). We can find a negative differential thermoelectric resistance (NDTR) in the system. The appearance of this physical phenomenon is due to the compensation effect of the thermal spin, which affirms the applicable use of the  $\alpha'$ -BNR in thermoelectric devices. For low temperatures  $T_R = 100$  K, the charge current is negative for all temperature differences, and in this state the current flows from the drain to the source while for higher temperatures, the charge current versus  $\Delta T$  and  $T_R$  increases linearly and flows from the source to the drain (see Fig. 7(f)).

In this study, we have examined the power factor (PF) as a key attribute for assessing the efficacy of materials in thermoelectric device applications. The charge and spin PF as a function of the Fermi energy for different temperatures has been represented in Fig. 8. The maximum value of the charge (spin) PF is decreased and widens by increasing the temperature. As we mentioned in Eq. 23, the spin Seebeck thermopower has an inverse relation with the temperature, thus by increasing the  $T$ , the spin thermopower is reduced, so the PF also decreases by enhancing the temperature. The charge and spin PFs in the vicinity of  $E_F = 0$

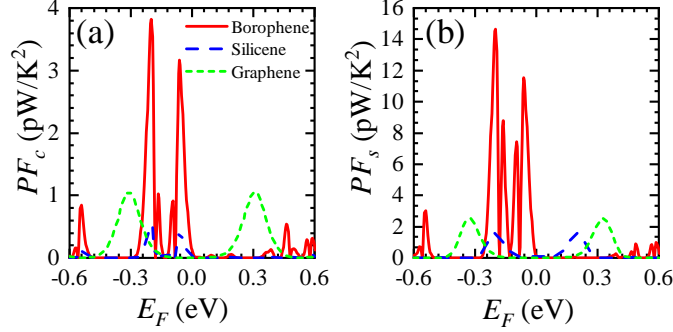


FIG. 9. (a) The charge and (b) spin power factors as a function of the Fermi energy for different nanoribbon such as  $\alpha'$ -boron, graphene and silicene. The temperature is  $T = 100$  K with  $N = 30$  atoms in the unit cell. The magnetisation is  $M_z = 0.098$  eV.

become larger where the thermoelectric effect is stronger in the range of  $-0.24 \text{ eV} < E < 0$ . Conversely, the charge and spin Seebeck thermopowers decrease as the inverse of  $T$  shows a decline in the power factors with temperature. Moreover, the spin PF of  $\alpha'$ -BNR is about four times greater than the charge PF, indicating that borophene has potential applications in spin thermoelectric devices. Finally, to reveal the high thermoelectric efficiency of  $\alpha'$ -BNR, we depicted the PF versus the Fermi energy for  $\alpha'$ -boron, graphene and silicene nanoribbons which is shown in Fig. 9. As seen, the charge (spin) PF of  $\alpha'$ -boron has the highest value  $0.56 \text{ pW/K}^2$  ( $1.12 \text{ pW/K}^2$ ) among of all, and this is due to the existence of a band gap and high asymmetry between electrons and holes in the  $\alpha'$ -boron nanoribbon. These results confirm the superior application of  $\alpha'$ -BNR in thermopower nanodevices.

#### IV. SUMMARY

We have investigated the spin-dependent conductance of the  $\alpha'$ -BNR through the proximity of ferromagnetic material with the right and left leads. All the calculations have been performed using the NEGF approach inside the TB model framework. Our designed system shows half-metallicity and spin-filtering characteristics by applying an exchange magnetic. We have also calculated the spin-dependent current using the Landauer-Büttiker formula. We find that by inducing temperature differences and breaking the electron-hole symmetry in the system, the spin-up and spin-down currents flow in opposite directions which shows a perfect spin current in the  $\alpha'$ -BNR and therefore it can act as an ideal spin-Seebeck diode.

Further, a negative differential spin-Seebeck effect through the compensation of thermal spin occurs in our device. Finally, we have studied the temperature effect on the efficiency of the  $\alpha'$ -BNR known as the charge and spin power factors. It is shown in the vicinity of the Fermi level, by increasing the temperature the maximum magnitude of the charge and spin PFs decreases dramatically because the thermopower is reduced. Furthermore, by comparing the the charge and spin PFs of  $\alpha'$ -boron, graphene and silicene nanoribbons, we found the former has the maximum value. Our results show that  $\alpha'$ -BNR can be a highly efficient material in thermoelectric devices.

- 
- [1] E. Elahi, A. A. Al-Kahtani, G. Dastgeer, S. Aftab, J. Aziz, M. W. Iqbal, M. Manzoor, J. Jeong, M. Suleman, B. Ahmed, *et al.*, *Appl. Mater. Today* **32**, 101846 (2023).
- [2] G. Yang, L. Sang, C. Zhang, N. Ye, A. Hamilton, M. S. Fuhrer, and X. Wang, *Nat. Rev. Phys.* **5**, 466 (2023).
- [3] K.-i. Uchida and R. Iguchi, *J. Phys. Soc. Jpn.* **90**, 122001 (2021).
- [4] A. Hirohata, K. Yamada, Y. Nakatani, I.-L. Prejbeanu, B. Diény, P. Pirro, and B. Hillebrands, *J. Magn. Magn. Mater.* **509**, 166711 (2020).
- [5] P. Dey and J. N. Roy, *Spintronics* (Springer, 2021).
- [6] S. Pawar, H. Duadi, and D. Fixler, *Nanomaterials* **13**, 598 (2023).
- [7] I. Žutić, J. Fabian, and S. D. Sarma, *Rev. Mod. Phys.* **76**, 323 (2004).
- [8] S. Wolf, D. Awschalom, R. Buhrman, J. Daughton, v. S. von Molnár, M. Roukes, A. Y. Chtchelkanova, and D. Treger, *science* **294**, 1488 (2001).
- [9] D.-D. Wu and H.-H. Fu, *Nanotechnology* **32**, 245703 (2021).
- [10] S. D. Bader and S. Parkin, *Annu. Rev. Condens. Matter Phys.* **1**, 71 (2010).
- [11] L. D. Hicks and M. S. Dresselhaus, *Phys. Rev. B* **47**, 12727 (1993).
- [12] M. Dresselhaus, Y. Lin, G. Dresselhaus, X. Sun, Z. Zhang, S. Cronin, T. Koga, and J. Ying, in *Eighteenth International Conference on Thermoelectrics. Proceedings, ICT'99 (Cat. No. 99TH8407)* (IEEE, 1999) pp. 92–99.
- [13] S. J. Heerema, L. Vicarelli, S. Pud, R. N. Schouten, H. W. Zandbergen, and C. Dekker, *ACS Nano* **12**, 2623 (2018).

- [14] Z. A. Piazza, H.-S. Hu, W.-L. Li, Y.-F. Zhao, J. Li, and L.-S. Wang, *Nat. Commun.* **5**, 3113 (2014).
- [15] D. Li, Y. Chen, J. He, Q. Tang, C. Zhong, and G. Ding, *Chin. Phys. B* **27**, 036303 (2018).
- [16] C. Hou, G. Tai, Y. Liu, Z. Wu, X. Liang, and X. Liu, *Nano Research Energy* **2**, e9120051 (2023).
- [17] A. P. Sergeeva, I. A. Popov, Z. A. Piazza, W.-L. Li, C. Romanescu, L.-S. Wang, and A. I. Boldyrev, *Acc. Chem. Res.* **47**, 1349 (2014).
- [18] A. J. Mannix, Z. Zhang, N. P. Guisinger, B. I. Yakobson, and M. C. Hersam, *Nat. Nanotechnol.* **13**, 444 (2018).
- [19] C. Hou, G. Tai, Z. Wu, and J. Hao, *ChemPlusChem* **85**, 2186 (2020).
- [20] M. Z. M. Nasir and M. Pumera, *TrAC, Trends Anal. Chem.* **121**, 115696 (2019).
- [21] Y. V. Kaneti, D. P. Benu, X. Xu, B. Yulianto, Y. Yamauchi, and D. Golberg, *Chem. Rev.* **122**, 1000 (2021).
- [22] Z. Zhang, E. S. Penev, and B. I. Yakobson, *Chem. Soc. Rev.* **46**, 6746 (2017).
- [23] X. Wu, J. Dai, Y. Zhao, Z. Zhuo, J. Yang, and X. C. Zeng, *ACS Nano* **6**, 7443 (2012).
- [24] T. Cheng, H. Lang, Z. Li, Z. Liu, and Z. Liu, *Phys. Chem. Chem. Phys.* **19**, 23942 (2017).
- [25] X. Chen, K. Fan, Y. Liu, Y. Li, X. Liu, W. Feng, and X. Wang, *Adv. Mater.* **34**, 2101665 (2022).
- [26] J.-J. Zhang, T. Altalhi, J.-H. Yang, and B. I. Yakobson, *Nanoscale* **13**, 8474 (2021).
- [27] H. Tang and S. Ismail-Beigi, *Phys. Rev. Lett.* **99**, 115501 (2007).
- [28] X. Yang, Y. Ding, and J. Ni, *Phys. Rev. B* **77**, 041402 (2008).
- [29] E. S. Penev, S. Bhowmick, A. Sadrzadeh, and B. I. Yakobson, *Nano Lett.* **12**, 2441 (2012).
- [30] H. Xiao, W. Cao, T. Ouyang, S. Guo, C. He, and J. Zhong, *Sci. Rep.* **7**, 45986 (2017).
- [31] C. Hou, G. Tai, Y. Liu, Z. Wu, Z. Wu, and X. Liang, *J. Mater. Chem. A* **9**, 13100 (2021).
- [32] C. Hou, G. Tai, J. Hao, L. Sheng, B. Liu, and Z. Wu, *Angew. Chem. Int. Ed.* **59**, 10819 (2020).
- [33] C. Hou, G. Tai, B. Liu, Z. Wu, and Y. Yin, *Nano Res.* , 1 (2021).
- [34] P. Sang, Q. Wang, W. Wei, Y. Li, and J. Chen, *ACS Appl. Nano Mater.* **4**, 11931 (2021).
- [35] D. C. Rodrigues, L. Lage, P. Venezuela, and A. Latgé, *Phys. Chem. Chem. Phys.* **24**, 9324 (2022).
- [36] Z.-X. Xie, X.-K. Chen, X. Yu, Y.-X. Deng, Y. Zhang, W.-X. Zhou, and P.-Z. Jia, *Comput. Mater. Sci* **220**, 112041 (2023).

- [37] E. Rahmati, A. Bafekry, M. Faraji, D. Gogva, C. V. Nguyen, and M. Ghergherehchi, RSC Adv. **12**, 6174 (2022).
- [38] J. Li, Y.-M. Niquet, and C. Delerue, Phys. Rev. B **107**, 245417 (2023).
- [39] X. Tan, L. Liu, G.-F. Du, and H.-H. Fu, Phys. Chem. Chem. Phys. **22**, 19100 (2020).
- [40] F. Ildarabadi and R. Farghadan, Phys. Rev. B **103**, 115424 (2021).
- [41] M. Markov, S. E. Rezaei, S. N. Sadeghi, K. Esfarjani, and M. Zebarjadi, Physical Review Materials **3**, 095401 (2019).
- [42] H. Haug, A.-P. Jauho, *et al.*, *Quantum kinetics in transport and optics of semiconductors*, Vol. 2 (Springer, 2008).
- [43] B. Bishnoi and B. Ghosh, RSC Adv. **3**, 26153 (2013).
- [44] M. L. Sancho, J. L. Sancho, and J. Rubio, J. Phys. F: Met. Phys. **14**, 1205 (1984).
- [45] T. Li and S.-P. Lu, Phys. Rev. B **77**, 085408 (2008).
- [46] M. B. Nardelli, Phys. Rev. B **60**, 7828 (1999).
- [47] S. Datta, *Quantum transport: atom to transistor* (Cambridge university press, 2005).
- [48] Y. Imry and R. Landauer, Rev. Mod. Phys. **71**, S306 (1999).
- [49] D. S. Fisher and P. A. Lee, Phys. Rev. B **23**, 6851 (1981).
- [50] Y. Meir and N. S. Wingreen, Phys. Rev. Lett. **68**, 2512 (1992).
- [51] U. Sivan and Y. Imry, Phys. Rev. B **33**, 551 (1986).
- [52] B. Z. Rameshti and A. G. Moghaddam, Physical Review B **91**, 155407 (2015).